Supplementary Material for LHCb-PAPER-2020-002

Fit projections of the control channel

The angular and mass distributions of $B^0 \to J/\psi K^{*0}$ candidates for the Run 1 and the 2016 data, along with the projections of the simultaneous fit, are shown in Fig. 1. The small level of disagreement between the data and the fit projection in $\cos\theta_K$ is attributed to contributions from $J/\psi\pi^-$ resonances that are not modelled in the fit (see Refs. [1, 2]).

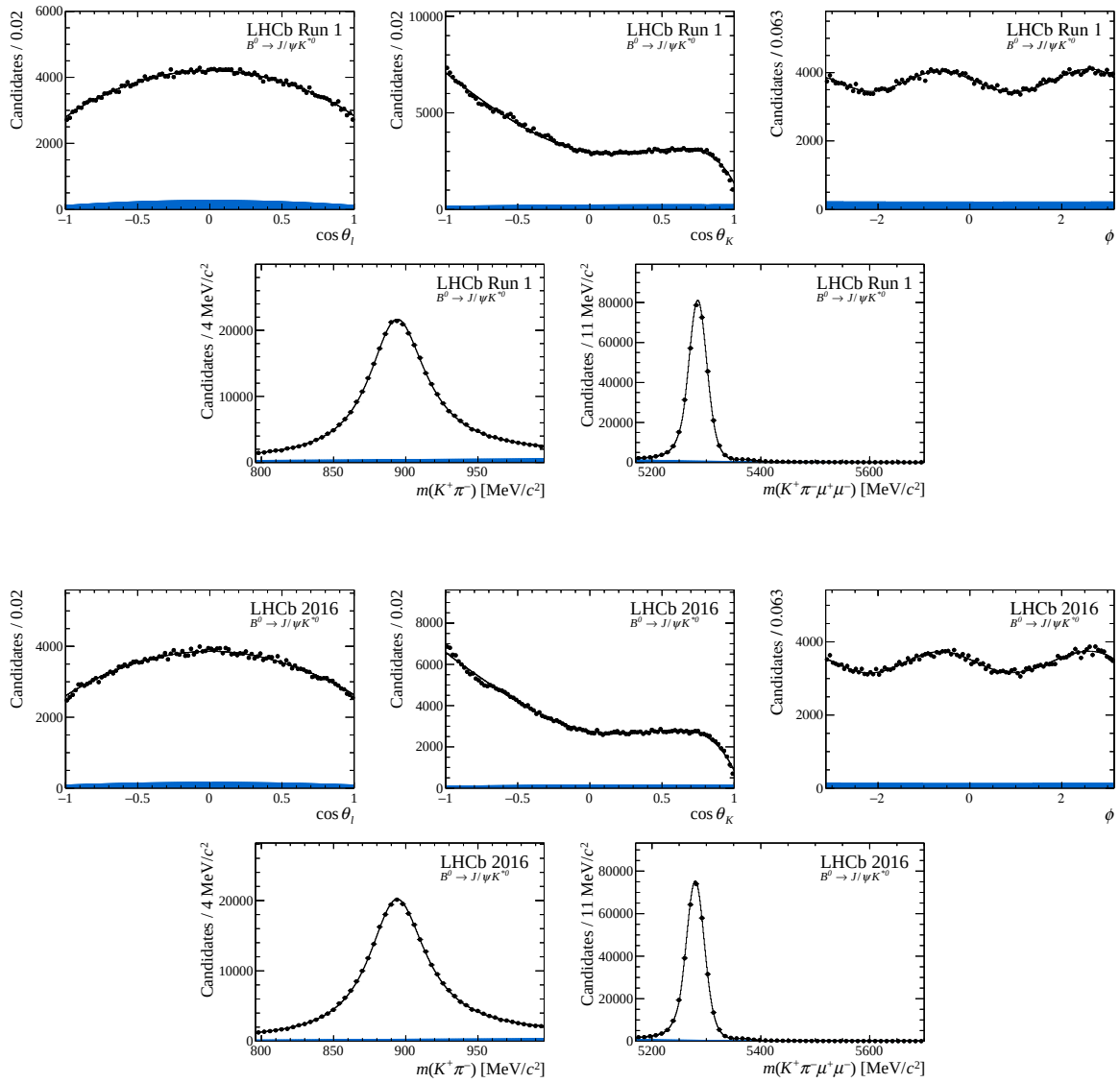

Figure 1: Projections of the fitted probability density function on the decay angles, $m(K^+\pi^-)$ and $m(K^+\pi^-\mu^+\mu^-)$ for the decay $B^0 \to J/\psi K^{*0}$. The blue shaded region indicates background.

Comparison of the Run 1 and the 2016 data

Results of the fit for the *CP*-averaged angular observables $F_{\rm L}$, $A_{\rm FB}$ and S_3–S_9 are compared to the Run 1 results from the previous analysis [3], as well as to the individual fit results of the 2016 data in Fig. 2. These figures are for illustrative purposes only, as the results shown for the 2016 data are not coverage- and bias-corrected, and the error bars do not include systematic uncertainties. An equivalent comparison is made for the $P_i^{(\prime)}$ basis in Fig. 3.

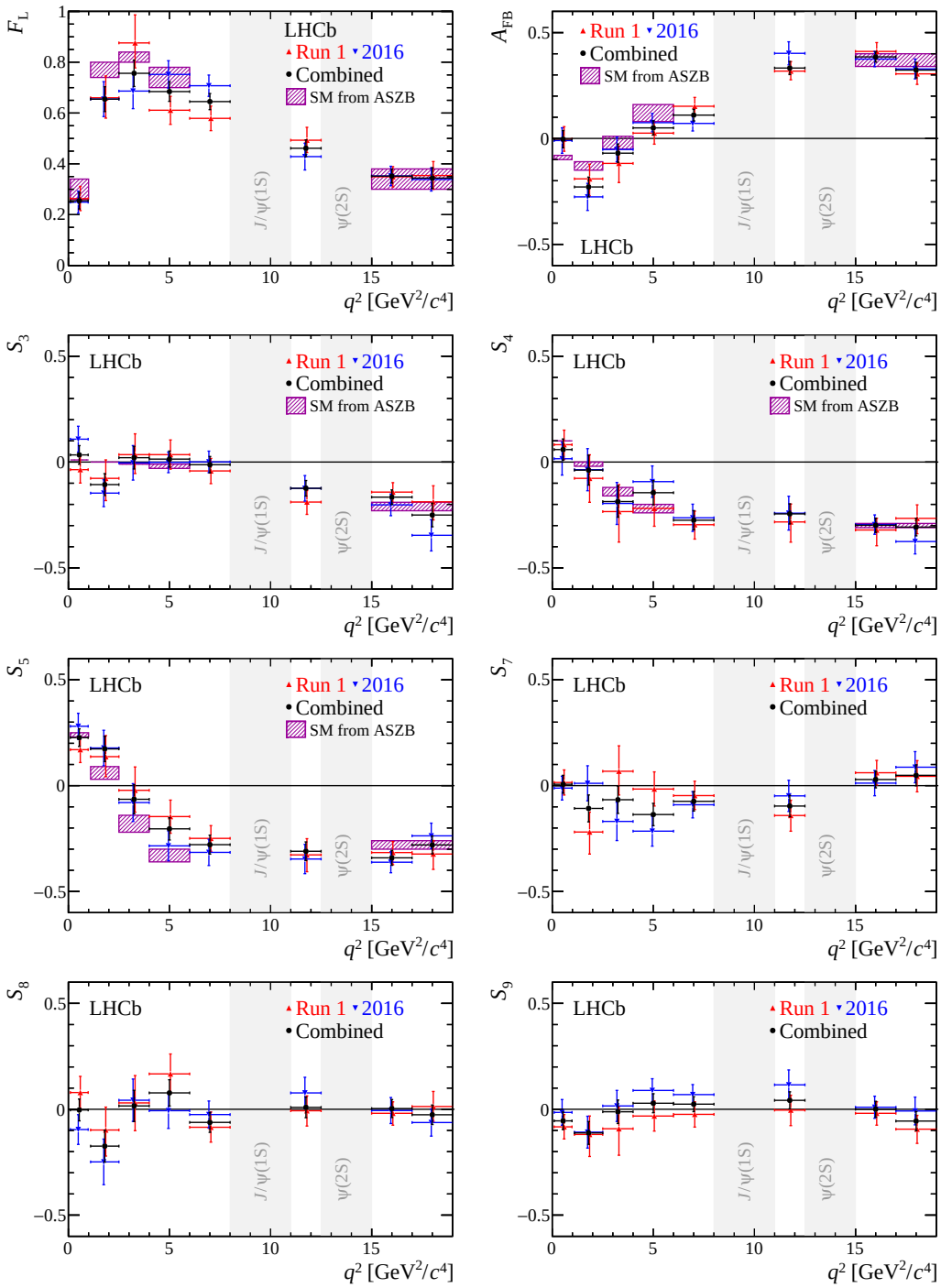

Figure 2: Results for the *CP*-averaged angular observables $F_{\rm L}$, $A_{\rm FB}$ and S_3–S_9 in bins of q^2 compared to the Run 1 results from the previous analysis [3], as well as the individual fit results for the 2016 data. The data are compared to SM predictions based on the prescription of Refs. [4,5]. These figures are for illustrative purposes only, as the results shown for the 2016 data are not coverage- and bias-corrected and the error bars do not include systematic uncertainties.

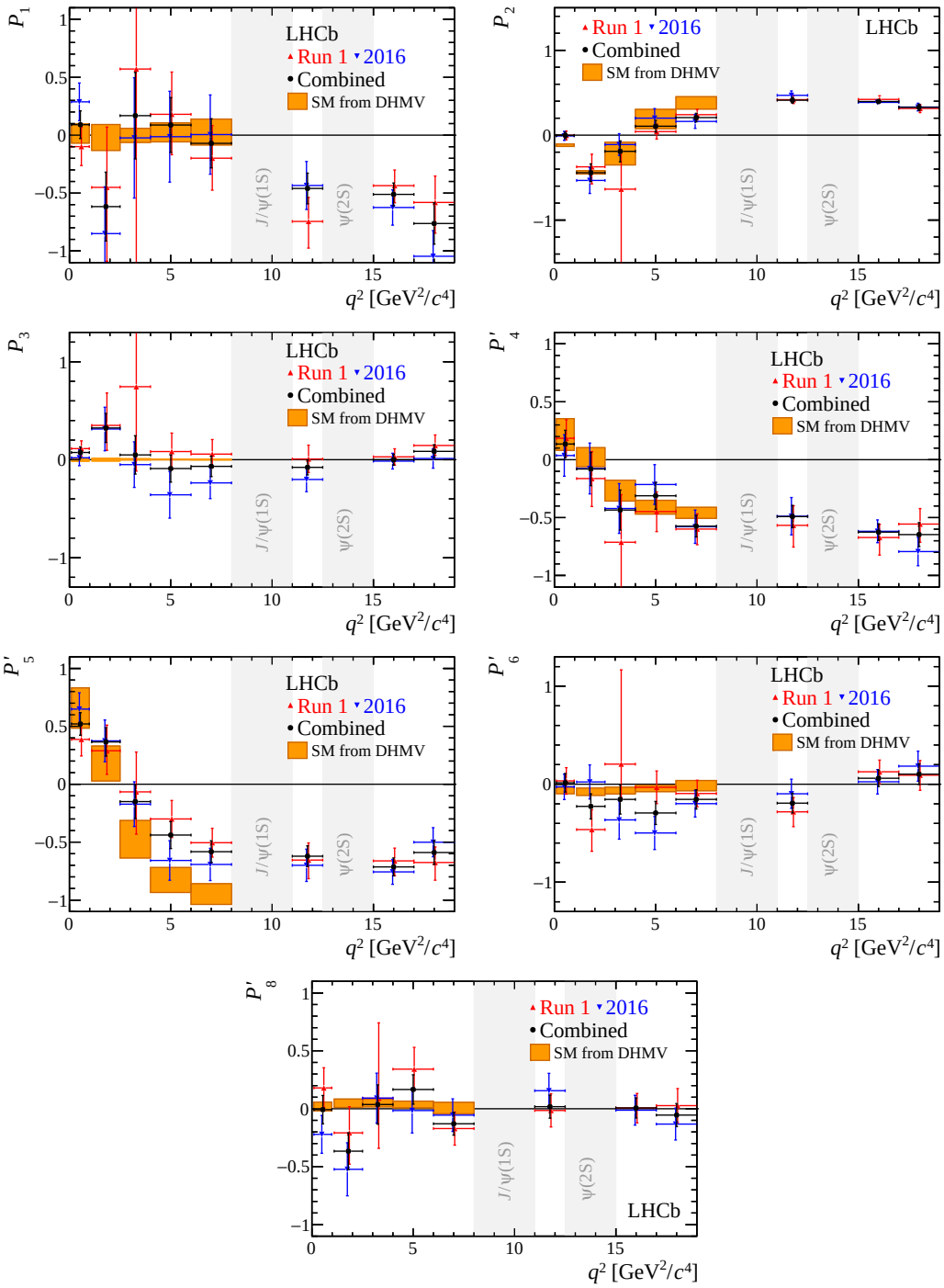

Figure 3: Results for the optimised angular observables P_1–P_3 and P'_4–P'_8 in bins of q^2 compared to the Run 1 results from the previous analysis [3], as well as the individual fit results for the 2016 data. The data are compared to SM predictions based on Refs. [6, 7]. These figures are for illustrative purposes only, as the results shown for the 2016 data are not coverage- and bias-corrected and the error bars do not include systematic uncertainties.

Comparison of the P_5' result to various physics scenarios

The results from the fit for the P_5' angular observable compared with the SM prediction and the predictions when shifting the effective coupling $\mathcal{R}e(C_9)$ are shown in Fig. 4. All predictions are obtained using the FLAVIO software package [8].

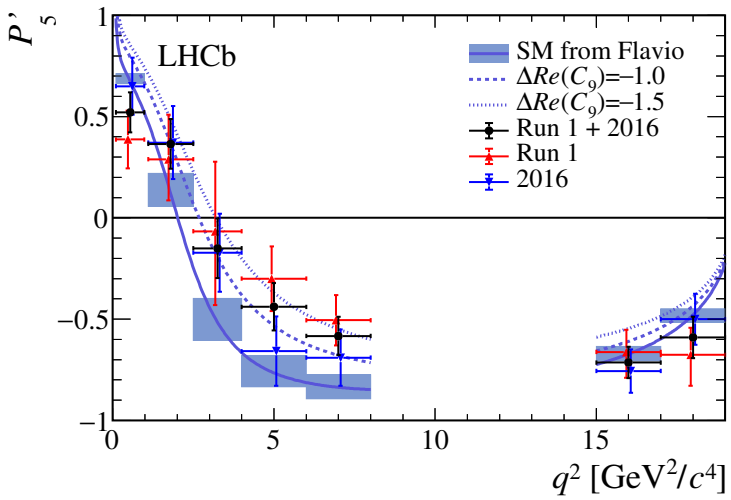

Figure 4: Observable P_5' compared with the SM prediction and with predictions that shift the effective coupling $\mathcal{R}e(C_9)$ by -1.0 and -1.5. All predictions are obtained using the FLAVIO software package [8].

2D fits to $\mathcal{R}e(C_9)$ and $\mathcal{R}e(C_{10})$

The FLAVIO software package is used to fit the *CP*-averaged angular observables, varying the real part of the vector coupling $\mathcal{R}e(C_9)$, the real part of the axial-vector coupling $\mathcal{R}e(C_{10})$ and the SM nuisance parameters. The q^2 bins included in the fit are the narrow q^2 bins in the ranges $0.10 < q^2 < 0.98\,\text{GeV}^2/c^4$, $1.1 < q^2 < 8.0\,\text{GeV}^2/c^4$ and the wide q^2 bin $15.0 < q^2 < 19.0\,\text{GeV}^2/c^4$. The contour plot obtained by fitting to the *CP*-averaged angular observables of the 2016 data set is shown for illustrative purposes only, as the *CP*-averaged angular observables are not coverage- and bias-corrected, and do not include systematic uncertainties.

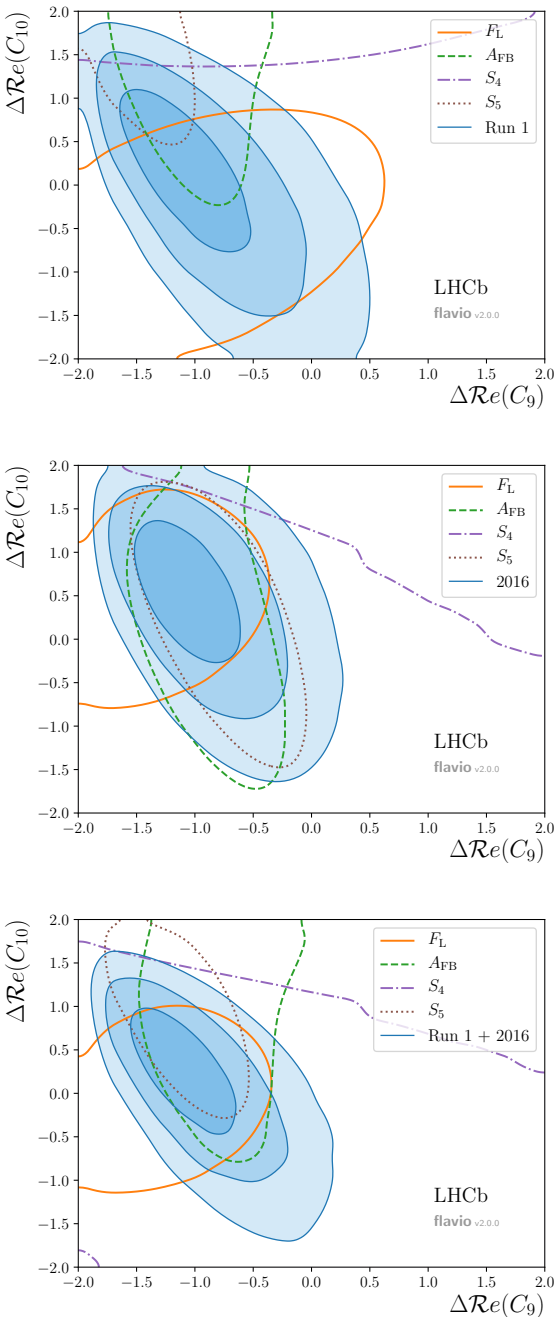

Figure 5: Fits to $\Delta\mathcal{R}e(C_9)$ and $\Delta\mathcal{R}e(C_{10})$, the shift in the values of $\mathcal{R}e(C_9)$ and $\mathcal{R}e(C_{10})$ from their SM values, using the results of the *CP*-averaged angular observables for Run 1, 2016 and the combined data set. The SM point lies at the origin. The blue lines show the $1, 2$ and $3\,\sigma$ contours of the fit to all angular observables. The other coloured lines show the 1σ contours of the fits to the individual angular observables. Those lines that cannot be seen in the plot correspond to angular observables for which the 1σ contours go beyond the range of the plots. The contour plot obtained by fitting to the *CP*-averaged angular observables of the 2016 data set is shown for illustrative purposes only, as the *CP*-averaged angular observables are not coverage- and bias-corrected, and do not include systematic uncertainties.

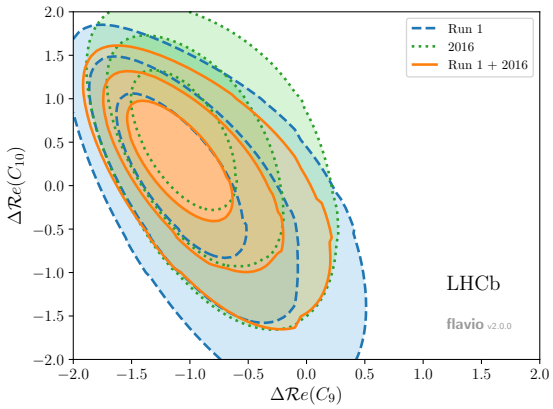

Figure 6: Fit to $\Delta\mathcal{R}e(C_9)$ and $\Delta\mathcal{R}e(C_{10})$, the shift in the values of $\mathcal{R}e(C_9)$ and $\mathcal{R}e(C_{10})$ from their SM values, using the results of the *CP*-averaged angular observables for Run 1, 2016 and the combined data set. The SM point lies at the origin. The lines show the $1, 2$ and $3\,\sigma$ contours of the fit to all angular observables. The contour plot obtained by fitting to the *CP*-averaged angular observables of the 2016 data set is shown for illustrative purposes only, as the *CP*-averaged angular observables are not coverage- and bias-corrected, and do not include systematic uncertainties.

1D fits to $\mathcal{R}e(C_9)$

The FLAVIO software package is used to perform a scan of the likelihood of the *CP*-averaged angular observables, varying the real part of the vector coupling $\mathcal{R}e(C_9)$. The q^2 bins included in the fit are the narrow q^2 bins in the ranges $0.10 < q^2 < 0.98\,\text{GeV}^2/c^4$, $1.1 < q^2 < 8.0\,\text{GeV}^2/c^4$ and the wide q^2 bin $15.0 < q^2 < 19.0\,\text{GeV}^2/c^4$.

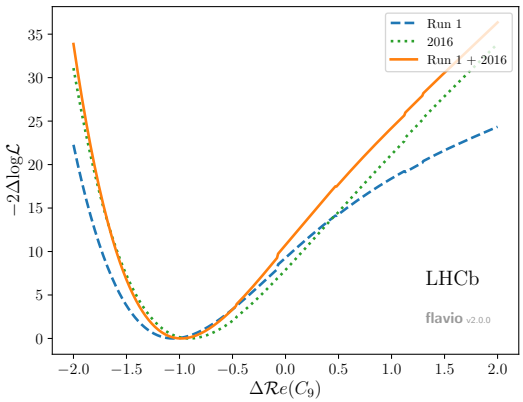

Figure 7: Likelihood scan of $\Delta\mathcal{R}e(C_9)$, the shift of $\mathcal{R}e(C_9)$ from its SM value, using the results of the *CP*-averaged angular observables for Run 1 only (blue dashed), 2016 only (green dotted) and the combined data set (solid orange). The result for the 2016 data set is shown for illustrative purposes only, as the *CP*-averaged angular observables are not coverage- and bias-corrected, and do not include systematic uncertainties.

References

[1] LHCb collaboration, R. Aaij *et al.*, *Model-independent observation of exotic contributions to $B^0 \to J/\psi K^+\pi^-$ decays*, Phys. Rev. Lett. **122** (2019) 152002, arXiv:1901.05745.

[2] Belle collaboration, K. Chilikin *et al.*, *Observation of a new charged charmonium like state in $\bar{B}^0 \to J/\psi K^-\pi^+$ decays*, Phys. Rev. **D90** (2014) 112009, arXiv:1408.6457.

[3] LHCb collaboration, R. Aaij *et al.*, *Angular analysis of the $B^0 \to K^{*0}\mu^+\mu^-$ decay using $3\,fb^{-1}$ of integrated luminosity*, JHEP **02** (2016) 104, arXiv:1512.04442.

[4] W. Altmannshofer and D. M. Straub, *New physics in $b \to s$ transitions after LHC run 1*, Eur. Phys. J. **C75** (2015) 382, arXiv:1411.3161.

[5] A. Bharucha, D. M. Straub, and R. Zwicky, *$B \to V\ell^+\ell^-$ in the Standard Model from light-cone sum rules*, JHEP **08** (2016) 098, arXiv:1503.05534.

[6] S. Descotes-Genon, L. Hofer, J. Matias, and J. Virto, *On the impact of power corrections in the prediction of $B \to K^*\mu^+\mu^-$ observables*, JHEP **12** (2014) 125, arXiv:1407.8526.

[7] A. Khodjamirian, T. Mannel, A. A. Pivovarov, and Y.-M. Wang, *Charm-loop effect in $B \to K^{(*)}\ell^+\ell^-$ and $B \to K^*\gamma$*, JHEP **09** (2010) 089, arXiv:1006.4945.

[8] D. M. Straub, *flavio: A python package for flavour and precision phenomenology in the Standard Model and beyond*, arXiv:1810.08132.